Eur. Phys. J. A **19**, 105–116 (2004)
DOI 10.1140/epja/i2002-10247-9

**THE EUROPEAN
PHYSICAL JOURNAL A**

Fragmentation of 95 MeV/u ^{12}C and 75 MeV/u ^{13}C. Application to secondary-beam production

G. Farès[1], R. Bimbot[2,a], S. Hachem[1], M. Mirea[3], R. Anne[4], T. Benfoughal[2], C. Cabot[2], F. Clapier[2], P. Delbourgo-Salvador[5], T. Ethvignot[5], A. Lefebvre[6], M. Lewitowicz[4], P. Roussel-Chomaz[4], M.G. Saint-Laurent[4], J.E. Sauvestre[5], J.L. Sida[7], and Yang Yong Feng[4]

[1] Université de Nice-Valrose, F-06108 Nice Cedex, France
[2] Institut de Physique Nucléaire; IN2P3/CNRS and UPS XI, F-91406 Orsay Cedex, France
[3] Institute of Atomic Physics, P.O. Box MG-6, Bucharest, Romania
[4] GANIL, BP 5027, F-14021 Caen Cedex, France
[5] DPTA/SPN, CEA, BP 12, F-91680 Bruyères le Châtel, France
[6] CSNSM; IN2P3/CNRS and UPS XI, F-91406 Orsay Cedex, France
[7] DAPNIA CEN Saclay, F-91191 Gif-sur-Yvette Cedex, France

Received: 17 September 2002 / Revised version: 25 July 2003 /

Communicated by W. Henning

Abstract. The fragmentation of 95 MeV/u ^{12}C and 75 MeV/u ^{13}C projectiles, interacting with natural targets of different elements (^{9}Be, $^{\mathrm{nat}}$Cu and ^{197}Au for ^{12}C, and ^{9}Be, $^{\mathrm{nat}}$Ni, and ^{181}Ta for ^{13}C) and of various thicknesses has been investigated at GANIL, using the doubly achromatic magnetic spectrometer LISE. The projectile-like fragments transmitted at 0° have been analysed using a silicon ΔE-E telescope and the ΔE–time-of-flight method. The results obtained with the thinnest targets are discussed in the scope of radioactive nuclear beam production. The fragment momentum distributions can be fitted by Gaussian peaks associated with exponential tails towards low momentum values. The experimental production yields are compared with the results of the simulation code LISE. It appears that this code reproduces satisfactorily the yields of nuclei close to the stability line, but strongly overestimates the production of very neutron-deficient nuclei.

PACS. 25.70.Mn Projectile and target fragmentation – 29.90.+r Other topics in elementary-particle and nuclear physics experimental methods and instrumentation

1 Introduction

Heavy-ion reactions leading to the observation of fragments of mass and velocity close to those of the projectile have now been observed for more than 20 years [1–3]. At relativistic energies, they are interpreted as "cold" projectile fragmentation [4,5]. In the energy domain concerned by this work (50–100 MeV/u), the situation is less clear, and many experiments have shown that the production of such fragments may occur through several competing processes ranging from elastic or inelastic transfer to projectile fragmentation followed by particle evaporation [6,7].

These reactions are interesting for understanding the mechanism of heavy-ion collisions, but also because they are currently used for producing secondary beams of radioactive isotopes. Such radioactive nuclear beams are produced and purified using in-flight spectrometers, both at relativistic energies (*e.g.*, at GSI Darmstadt) and at energies lower than 100 MeV/u (*e.g.*, at GANIL, MSU and RIKEN). Simulation codes have been elaborated to predict the experimental conditions for obtaining the highest intensity for a given secondary beam. However, precise measurements of projectile fragment production at zero degrees are scarce, and systematic measurements do not exist. The present work is part of a study which aims at collecting basic data concerning these fragmentation reactions induced by various projectiles from C to Ni in various targets (from Be to Au). Experimental momentum distributions and production yields for a series of radioactive beams have been obtained using a magnetic spectrometer with a large $B\rho$ acceptance. These data, which have

---

[a] e-mail: `bimbot@ipno.in2p3.fr`

Table 1. Projectile-target combinations used for the present experiment. The symbol t refers to the target thickness, $\Delta E/E$ is the relative energy loss in the target, and E_{mid} the beam energy in the mid-plane of the target.

^{12}C beam			
Targets	t (mg/cm^2)	$\Delta E/E$ (%)	E_{mid} (MeV/u)
Be	44.5	0.9	94.6
Cu	47.2	0.8	94.6
Au	97	1.2	94.4
Be	764	16	87.4
Cu	785	13	88.7
Au	1141	14	88.2
Be	1710	40	76.1
Cu	2064	38	76.8
Au	2845	40	76.1

^{13}C beam			
Targets	t (mg/cm^2)	$\Delta E/E$ (%)	E_{mid} (MeV/u)
Be	44.5	1.2	74.5
Ni	32	0.8	74.7
Ta	133	2.3	74.1
Be	–	–	–
Ni	451	11	70.9
Ta	578	10	71.2
Be	1441	50	56.4
Ni	868	22	66.7
Ta	1173	21.4	67

been presented in internal publications [8–12] will be useful to improve the existing parametrisations. They may also serve as a basis for comparison with future models, as the fragmentation process at such energies is not completely understood.

The present paper concerns the results obtained with 95 MeV/u ^{12}C and 75 MeV/u ^{13}C. These projectiles present an additional interest as it is now well established that carbon beams are among the best tools for hadrontherapy, *i.e.* radiotherapy with beams of particles heavier than electrons [13]. It is therefore important to know the production rates and momenta of secondary fragments emitted around zero degrees by carbon ions travelling through matter. Indeed, such fragments may perturb the treatment, as their range is often higher than that of the primary beam. On the other hand, among them, the β^+-emitters can be used for visualizing the Bragg peak position, using a special version of the PET camera. This last technique requires the knowledge of the production rates for such fragments, and of their momentum distributions, particularly along the beam direction, in order to compare their range with that of the primary beam.

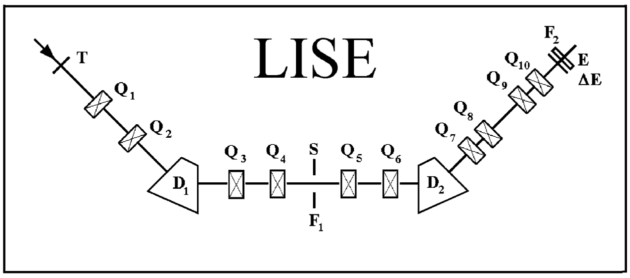

Fig. 1. Sketch of the LISE spectrometer at GANIL. The symbols Q refer to quadrupoles. The dipoles are denoted by D and the achromatic focal points by F.

2 Experimental procedure

2.1 Primary beams and targets

The experiments were performed at GANIL, according to a method initiated in refs. [14,15]. Beams of ^{12}C and ^{13}C were used as projectiles. Their fragmentation was induced by collisions with targets of several elements and of several thicknesses. The characteristics of the beams and targets used are given in table 1. The target thickness corresponded to energy losses of the primary beams approximately equal to 1%, 15% and 40% of the incident energy.

The primary-beam intensity was measured using a secondary emission probe, monitored for each experiment by comparison with a Faraday cup. In this work, primary-beam intensities were varied from 0.1 to 100 nAe.

2.2 Secondary-beam selection

The secondary nuclei from projectile fragmentation were separated and transported over 18 meters by the doubly achromatic spectrometer LISE [16]. Then, they were detected at the achromatic focal point of the spectrometer, using a telescope made of two silicon detectors, ΔE (300 μm) and E (1000 μm).

A sketch of the LISE spectrometer is given in fig. 1. The preparation of secondary beams using this device is performed according to the following principles:

The first section of LISE, composed of the dipole D_1 and of the quadrupoles Q_1 to Q_4 is used to select the nuclei produced in the target T according to their magnetic rigidity:

$$B \cdot \rho = 0.1438\, A/q \left[E/A(1 + E/2Auc^2)\right]^{1/2}, \qquad (1)$$

in which B (T) is the magnetic field in the dipole D_1, ρ (m) the average curvature radius of the trajectories in D_1, A (u) the mass of the selected ion, q its ionic charge (practically always equal to the atomic number Z in the present experiment), E (MeV) its kinetic energy, and $uc^2 = 931.5$ is the mass unit, expressed in MeV.

The reaction products emitted around 0°, within the spectrometer angular acceptance, are dispersed as A/q (*i.e.* A/Z in this experiment) in the focal plane F_1 of the

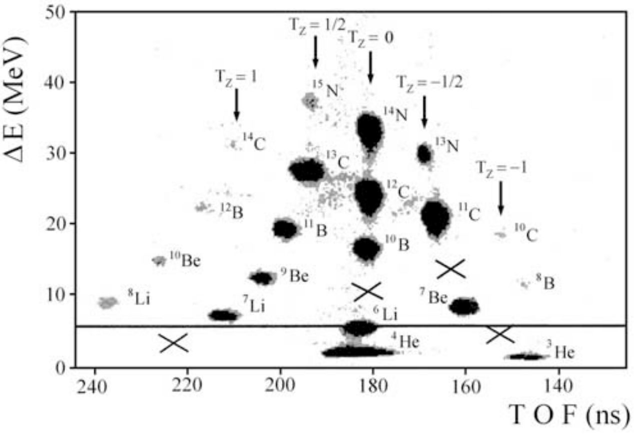

Fig. 2. Example of bidimensional plot used for isotope identification. The crosses indicate the missing nuclei ^{5}He, ^{5}Li, ^{8}Be and ^{9}B. The horizontal line is produced with an electronic pulse generator, the amplitude of which is set here to simulate the calculated energy loss of ^{6}Li. These pulses are used to check the electronic stability, and to verify the isotope identification.

dipole D_1, where a slit S is used to select them according to their momentum. The momentum acceptance is given by

$$\Delta p/p(\%) = a/D\,,$$

where a (mm) is the slit aperture and D (mm/%) the dispersion, which depends on the tuning up of the spectrometer elements. In the present work, the choice of the experimental parameters $a = 20$ mm, $D = 16.74$ mm/% led to a total momentum acceptance of 1.2%.

The second section of LISE is composed of the dipole D_2 and of the quadrupoles Q_5 to Q_{10}. Its first part (D_2, Q_5 and Q_6) compensates the dispersion of the first section and insures a double achromatism, in angle and position. Finally, the quadrupole lenses Q_7 to Q_{10} are used to focus the products at the final focal point F_2 where they are identified and counted with a telescope of silicon detectors. In order to preserve the detector resolution, the counting rate in the telescope is limited to less than a few thousand per second. The secondary-beam position, size and intensity can be monitored in various points of interest along the spectrometer line using a set of secondary emission probes, ionisation profilers, and Faraday cups.

2.3 Data analysis and identification

The identification of the isotopes present in the secondary beam selected by the spectrometer is obtained by using a bidimensional plot of the energy loss (ΔE) *versus* the time of flight (TOF) of the fragment. An example of ΔE–TOF plot is given in fig. 2. The line of constant TOF, observed in the centre of the bidimensional representation ΔE *vs.* TOF, corresponds to isotopes with $A/Z = 1/2$, *i.e.* with the isospin projection $T_Z = 0$. Lines corresponding to other values of T_Z are no more vertical, but they are clearly visible. For example, the line $T_Z = 1/2$ goes from ^{15}N to ^{7}Li. The existence of such lines, combined with the absence of the well-known unbound nuclei, such as ^{8}Be ($T_Z = 0$) and ^{9}B ($T_Z = -1/2$) permits the absolute calibration of Z and A to be readily established.

3 Results and discussion

This part will mainly focus on the results obtained using thin targets, as they are not significantly influenced by the subsequent fragment interaction with the target. After a general presentation showing that these data are coherent with previous results, they will be discussed in the scope of parametrizing the production yields and momentum distributions. Finally, these data will be used for testing the last version of the simulation code LISE.

3.1 General presentation of the data

For a given setting of the spectrometer, and in particular for a given value of the magnetic field B, the individual production yields are obtained by dividing the intensity I counted in the telescope for each isotope by the primary-beam intensity I_0. For each of the beam-target couples used in this experiment, and for each isotope produced, the individual production rate I/I_0 can thus be plotted *versus* the magnetic rigidity $B\rho$. The $B\rho$ values covered by these experiments range from 1.4 to 3.2 T m. The complete set of results concerning the individual production rates of all observed isotopes from the interaction of 95 MeV/u ^{12}C and 75 MeV/u ^{13}C with the targets listed in table 1 are presented in ref. [8]. Only a few typical examples will be given here. The first ones concern a 44.5 mg/cm^2 Be target bombarded by both ions. The corresponding individual production yields I/I_0 are presented as a function of $B\rho$ in figs. 3 and 4. In order to make the comparisons easier, these values have also been plotted *versus* B/B_0, B_0 denoting the magnetic-field value which corresponds to the transmission, through the spectrometer, of the primary beam exiting the target. In figs. 3 and 4, the left scale of the ordinates corresponds to the differential cross-sections $\mathrm{d}^2\sigma/[\mathrm{d}\Omega(\mathrm{d}p/p)]$, which are proportional to the I/I_0 values (right side of the ordinate scales) through the following equation:

$$\frac{\mathrm{d}^2\sigma}{\mathrm{d}\Omega\mathrm{d}p/p} = 1.66\cdot 10^6\frac{A}{t}\frac{1}{\Delta\Omega}\frac{D}{a}\frac{I}{I_0} \qquad (2)$$

In eq. (2), A (in u) and t (in mg/cm^2) are the atomic mass and thickness of the target, $\Delta\Omega = 1$ msr is the LISE solid angle, D and a have been already defined. The coefficient $1.66\cdot 10^6$ is the inverse of the Avogadro number multiplied by a factor 10^{18} for adjusting the units to mb/(msr %).

From the observation of figs. 3 and 4, it is clear that the production cross-sections are the highest for the stable nuclei close to the projectile. The production yields are much smaller for projectile fragments lying far from the

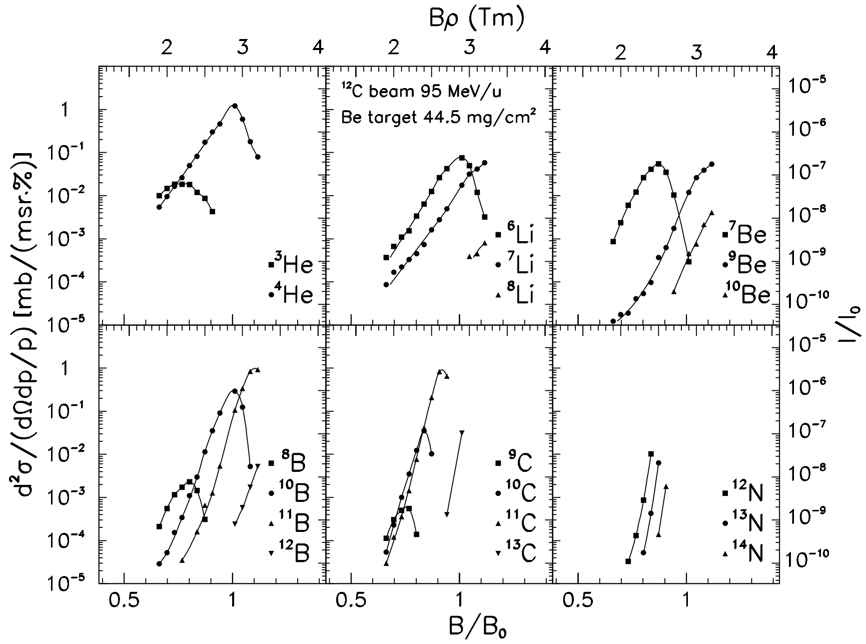

Fig. 3. Fragment production from the interaction of 95 MeV/u ^{12}C ions with a 44.5 mg/cm^2 target of ^{9}Be. The individual production yields I/I_0 and the corresponding double differential cross-sections are plotted *versus* the magnetic rigidity $B\rho$. The lower abscissa scale is relative to the ratio B/B_0 (see text for the definition of B_0). The symbols represent the experimental results obtained for the production of the indicated nuclei. The error bars are statistical and are generally smaller than these symbols. The solid lines are drawn to guide the eye.

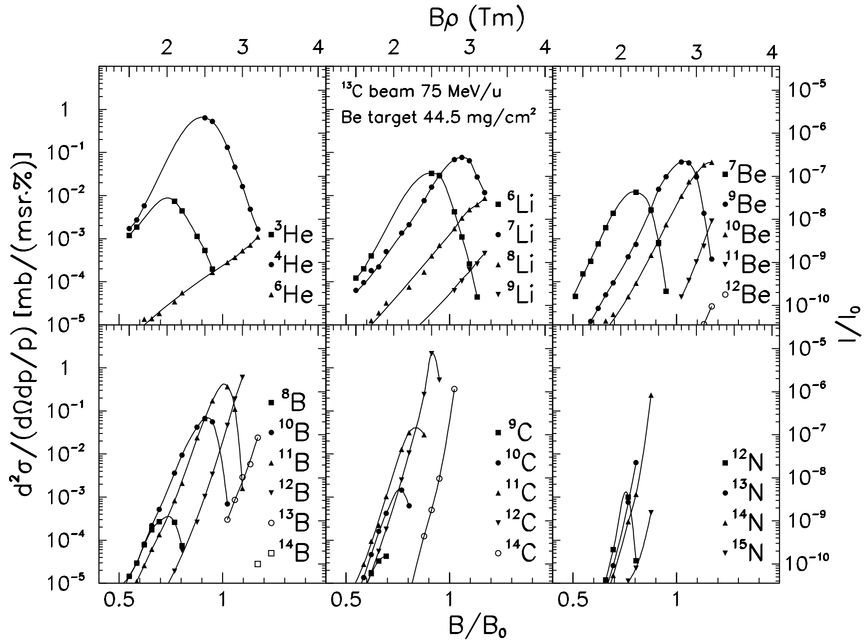

Fig. 4. Same as fig. 3 for the interaction of 75 MeV/u ^{13}C ions with a 44.5 mg/cm^2 target of ^{9}Be.

stability such as ^{8}B and ^{9}C. Moreover, even for fragments near the stability line, a lower differential cross-section is observed when their mass A_{f} is close to $A_{\mathrm{P}}/2$, the term A_{P} denoting the projectile mass. By comparing figs. 3 and 4, it is also clear that more species are observed when the projectile is ^{13}C than when it is ^{12}C. A detailed comparison between the results obtained with these two projectiles will be presented in section 3.3.

3.2 Momentum distributions

As the $B\rho$ distributions shown in figs. 3, 4 have been measured at 0° relative to the beam direction, they can be easily converted into the parallel momentum distributions of the fragments. Such distributions are presented in fig. 5 for ^{12}C- and ^{13}C-induced reactions in the thinnest Be target. They exhibit an asymmetric shape with a maximum

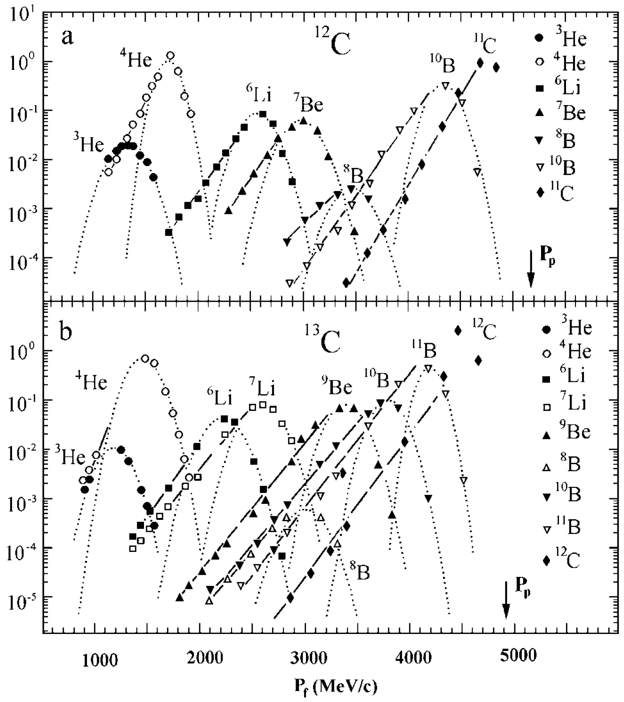

Fig. 5. Parallel-momentum distributions for projectile-like fragments produced by beams of 95 MeV/u^{12}C (a) and 75 MeV/u ^{13}C (b) with a ^{9}Be target of 44.5 mg/cm^2. The dotted and dashed lines are, respectively, Gaussian and exponential fits of the data (solid symbols). The arrows correspond to the momentum of the beam.

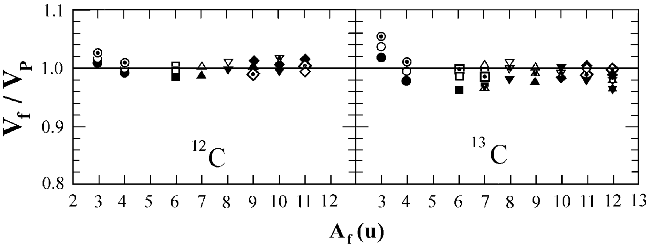

Fig. 6. Ratio of the most probable fragment velocity to the projectile one, plotted *versus* the fragment mass, for incident ^{12}C at 95 MeV/u (left panel), and ^{13}C at 75 MeV/u (right panel). For ^{12}C, the data correspond to targets of 44.5 mg/cm^2 Be (closed symbols), 47.2 mg/cm^2 Cu (open symbols), and 97 mg/cm^2 Au (dotted symbols). For ^{13}C, the data correspond to targets of 44.5 mg/cm^2 Be (closed symbols), 32 mg/cm^2 Ni (open symbols), and 133 mg/cm^2 Ta (dotted symbols). As far as the fragment Z's are concerned, circles correspond to He, squares to Li, triangles to Be, inverted triangles to B, lozenges to C and stars to N. A line is drawn for $V_f/V_P = 1$.

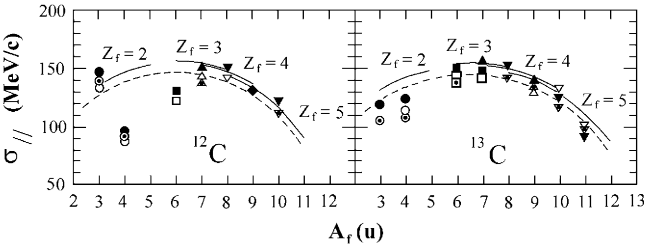

Fig. 7. Widths of the parallel-momentum distributions, plotted *versus* the fragment mass, for incident ^{12}C at 95 MeV/u (left panel), and ^{13}C at 75 MeV/u (right panel). The symbols are as in fig. 6. These data are compared to the Goldhaber prediction uncorrected (broken line) and corrected for a final-state Coulomb interaction (solid lines).

on the high-momentum side followed by a slow decrease (tail) towards low momentum values. Such asymmetric distributions may be decomposed into two components, a Gaussian one, which corresponds to their high-momentum part, and an exponential tail.

3.2.1 High-momentum component

The high-momentum component can be determined in reference to the cold-fragmentation model [4,5] which assumes a Gaussian distribution for the fragment longitudinal momentum $p_{\parallel}$:

$$\frac{d^2\sigma}{d\Omega dp} \propto \exp\left[-\frac{(p_{\parallel} - \langle p_{\parallel}\rangle)^2}{2\sigma_{\parallel}^2}\right]. \qquad (3)$$

In eq. (3), $\langle p_{\parallel}\rangle$ denotes the average parallel momentum and $\sigma_{\parallel}$ is the width of the longitudinal-momentum distribution. The high-momentum side is therefore fitted by a Gaussian function (dotted line). The center of this Gaussian yields the $\langle p_{\parallel}\rangle$ value, linked to the most probable fragment velocity, and its width yields the $\sigma_{\parallel}$ value.

As one can see in fig. 6, the present results confirm the observation of several authors that the most probable fragment velocity V_f of the fragments emitted around zero degrees is very close to the beam velocity V_P [7]. Indeed, if one excepts the He fragments for which the production mechanism is probably different, the measured ratio V_f/V_P is very close to unity with a slow decrease with decreasing fragment mass. Note that the uncertainty in the determination of this ratio is about 2 to 5% . Therefore, the small differences observed for the same isotope from one target to another are not significant. For the same reason, some of the experimental values of V_f/V_P appear to be higher than unity while the general trend is that all the fragment velocities are lower than the projectile one.

For parametrization purposes, the recommendation coming from these results is that, for projectiles and fragments in this mass range, the approximation $V_f = V_P$ is reasonably good. Note that this result is in qualitative agreement with both a cold fragmentation and a transfer process.

The widths $\sigma_{\parallel}$ of the parallel-momentum distributions of fragments, determined from the experimental momentum spectra, are plotted in fig. 7 as a function of the fragment mass for ^{12}C- and ^{13}C-induced reactions in the thinnest targets. These values are compared to those deduced from the simple fragmentation scheme established by Goldhaber [4] which reproduces the parallel-momentum distribution widths at high energy fairly well.

Let us recall that, in the framework of this statistical approach, in which the projectile is made up of A_P independent nucleons, the fragment momentum distribution is Gaussian with a width given by the parabolic law

$$\sigma_\parallel^2 = \sigma_0^2 \frac{A_\mathrm{f}(A_\mathrm{P} - A_\mathrm{f})}{A_\mathrm{P} - 1}\,. \tag{4}$$

In eq. (4), the term σ_0 is the reduced width. It is linked to the average momentum of the missing nucleons in the projectile fragment. In a first approach, it can be related to the Fermi momentum p_Fermi of the nucleons inside the projectile:

$$\sigma_0^2 = \frac{p_\mathrm{Fermi}^2}{5}\,. \tag{5}$$

For projectiles lighter than argon, this approximation leads to values of σ_0 in the range 100–110 MeV/c, but the early works on this theme showed that a better agreement was obtained with experiment for lower values of this parameter (80–90 MeV/c). This deviation was explained by Bertsch [17] by taking into account the fact that the missing nucleons are localized in space. Due to the Pauli principle, the momenta of these individual nucleons are correlated, and this reduces the parameter σ_0 by about 20%.

The values of $\sigma_\parallel$ indicated in fig. 7 by the dashed line have been calculated with $\sigma_0 = 81$ MeV/c for 95 MeV/u ^{12}C and $\sigma_0 = 77$ MeV/c for 75 MeV/u ^{13}C, which represent the best fit to the present data, if one excludes the ^{4}He fragments for both projectiles and ^{6}Li fragments for incident ^{12}C (see below). Note that these σ_0 values are in fair agreement with the interpretation given above.

The $\sigma_\parallel$ values can be corrected by adding to $\sigma_\parallel^2$ the term $1/3\ (Z_\mathrm{P} - Z_\mathrm{f})C_0^2$ representing the contribution from a Coulomb final-state interaction between the fragment and the protons dissociated from the projectile [18]. The parameter C_0 is equal to

$$C_0 = \sqrt{\frac{2m_\mathrm{p} Z_\mathrm{f} e^2 A_\mathrm{f}}{r_0 A^{1/3}(A_\mathrm{f} + 1)}}\,,$$

where m_p is the mass of a proton, and $r_0 = 1$ fm.

As can be seen in fig. 7, this charge effect is small and does not influence the overall agreement of the parametrization with the data. However, one should record that this result only concerns the momentum dispersion in the longitudinal direction. This charge effect plays a more significant role in the transverse direction as it is accompanied by the orbital deflection of the projectile in the field of the target nucleus [18–21].

The above-mentioned particular behaviour of ^{4}He is not surprising, as this nucleus can be produced through many processes. In particular, when the projectile is ^{12}C, the very low $\sigma_\parallel$ values observed for this fragment may be due to projectile break-up into three alpha-particles, a process which is not taken into account in the picture of Goldhaber. In the same way, the reduced width values observed for $A_\mathrm{f} = 6$, but only when the projectile is ^{12}C, could be explained by the break-up of this projectile into two ^{6}Li nuclei.

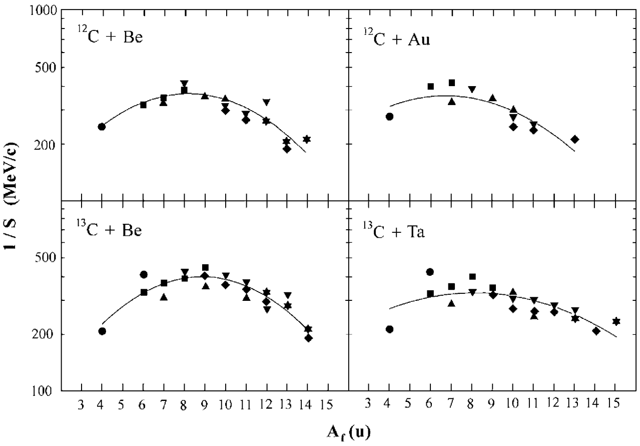

Fig. 8. Inverse of the slope obtained from the exponential fit of the parallel-momentum distributions shown in fig. 5, plotted *versus* the fragment mass. The projectile-target couple is indicated in each plot. The fragment Z's are represented by different symbols, as in fig. 6. The solid lines are drawn to guide the eye.

3.2.2 Low-momentum tail

The tail observed in fig. 5 on the low-momentum side of the curves may be interpreted as an indication of the presence of an energy dissipation process such as nucleon evaporation following a transfer or fragmentation step. For example, the tail in the ^{6}Li distribution could contain events corresponding to one neutron evaporation by an excited ^{7}Li fragment. As indicated by the dashed line in fig. 5, this low-momentum component is quite consistent with an exponential function. The slope of this exponential function appears to vary with the fragment mass A_f. In order to demonstrate this variation, and to give elements for parametrizing the slope s, the evolution of the inverse of this slope *versus* A_f is represented in fig. 8 for ^{12}C and ^{13}C ions impinging on targets of (Be, Au) and (Be, Ta), respectively. A maximum is observed (for the inverse of the slope) for fragments having masses between 6 and 9 u. This corresponds to a minimum for the slope. In other words, for these fragments the distributions extend more towards low energies. This means that the dissipation processes ("hot fragmentation" or inelastic transfer) are relatively important. On the contrary, for fragments close to the projectile, the dissipation is reduced. This means that the processes of quasielastic transfer and cold fragmentation are predominant for these nuclei [22].

3.3 Production yields

3.3.1 Influence of the projectile

In order to compare isotope production from the interaction of ^{12}C and of ^{13}C with a Be target, the yields $\mathrm{d}\sigma/\mathrm{d}\Omega$ for various nuclides, obtained by integration of the $B\rho$ distributions over the whole $B\rho$ range, are plotted i) in fig. 9a *versus* the fragment isospin projection $(T_Z)_\mathrm{f}$, and ii) in

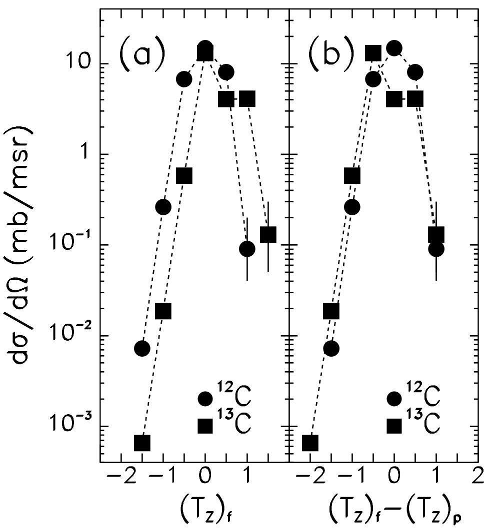

Fig. 9. Influence of the projectile on the fragment production at zero degrees, for a 44.5 mg/cm^2 target of ^{9}Be. Comparison ^{12}C/^{13}C. a) Differential cross-sections at zero degrees as a function of the fragment isospin $(T_Z)_f$. b) Differential cross-sections at zero degrees as a function of the difference between the fragment and the projectile isospins $(T_Z)_f - (T_Z)_P$.

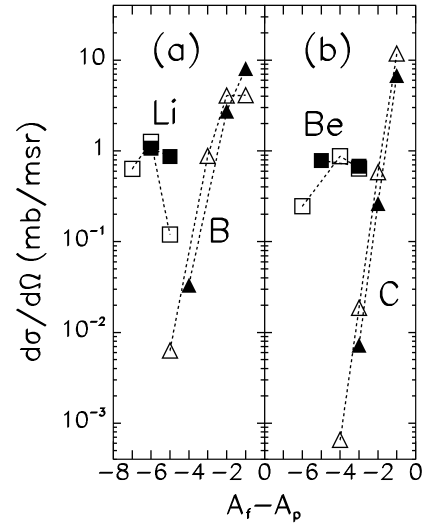

Fig. 10. Influence of the projectile on the fragment production at zero degrees, for a 44.5 mg/cm^2 target of ^{9}Be. The differential cross-sections at zero degrees are plotted *versus* the difference between the fragment and the projectile masses $A_f - A_P$. The open symbols correspond to ^{12}C projectiles, the closed ones to ^{13}C. a) Li and B fragments; b) Be and C fragments.

fig. 9b *versus* the difference ΔT_Z between the projectile and fragment isospin projections $[\Delta T_Z = (T_Z)_f - (T_Z)_P]$. One can see from fig. 9a that the ^{12}C projectile is more productive than ^{13}C for fragments with $(T_Z)_f < 0$, and less productive for fragments with $(T_Z)_f > 1/2$. Note that the fragments produced through elastic or inelastic scattering of the projectile are not taken into account in the results shown in this figure. This leads to an underestimation of fragments with $(T_Z)_f = 0$ when ^{12}C is the projectile and of fragments with $(T_Z)_f = 1/2$ when ^{13}C is the projectile. Finally, one may conclude from fig. 9a that, as expected, the more neutron-rich beam leads to the more neutron-rich fragments. More precisely, it can be seen in fig. 9b that the fragment production in governed by the difference between the isospin projection of the projectile $(T_Z)_P$ and of the fragment $(T_Z)_f$. The distribution of fig. 9b, which exhibits a quasi-Gaussian shape centered on $\Delta T_Z = 0$, can be used as a guide for the parametrization of secondary-beam production.

As several fragments have the same isospin, it is interesting to check whether this global property is also valid for each individual fragment, *i.e.* whether the isotopic production curves corresponding to ^{12}C projectiles are shifted by one unit relative to the ^{13}C ones for a given value of the fragment charge Z_f. In that purpose, the production yields are presented *versus* $\Delta A = A_f - A_P$. This is done in fig. 10 (a and b) for Li, Be, B and C isotopes. It is clear from this figure that this quantity ΔA, which reflects the number of nucleons lost by the projectile, is a key parameter governing the production of secondary beams.

3.3.2 Influence of the target nature

The influence of the target nature on the production rates may be appreciated in fig. 11 in which the experimental yields of various isotopes are compared for targets of Be, Cu and Au of equivalent thickness relative to the beam slowing-down, *i.e.* corresponding to the same energy loss for the beam. From the right scale of this figure, one can see that the differential isotope yield I/I_0 decreases when the target atomic number increases. At the same time, one can see on the left scale that the differential cross-section is almost independent of the target. This result is made clearer by comparing, in fig. 12, the secondary-fragment production yield at zero degrees Y/I_0, obtained by integrating I/I_0 over the whole range of $B\rho$ values, for three targets of equivalent thickness, bombarded by a ^{13}C beam. In fig. 12, the values Y/I_0 are plotted *versus* the fragment mass. (Note that a given mass may correspond to one or several nuclides of different Z.) Two features emerge from this figure. Firstly, all the curves exhibit similar shapes, *i.e.* a regular decrease from mass 12 to mass 3 with two accidents corresponding to the masses 8 and 4. (There is no stable nucleus at mass 5.) The dip observed at mass 8 corresponds to the instability of ^{8}Be which decays immediately into two ^{4}He. The nucleus ^{9}B is also unstable, but its absence is probably hidden by a substantial production of its isobares, and particularly ^{9}Be. The maximum at mass 4 corresponds to the fact that this nucleus (^{4}He) may be produced through many processes among which the decay of ^{8}Be and ^{9}B.

Secondly, although the targets do not strictly correspond to the same projectile energy loss, the data displayed in fig. 12 indicate that the production in the Be target is much higher than that in Ni, which is itself higher than the production in Ta. This is due to a trivial effect: light targets contain more atoms than heavy targets when their thicknesses correspond to the same projectile energy

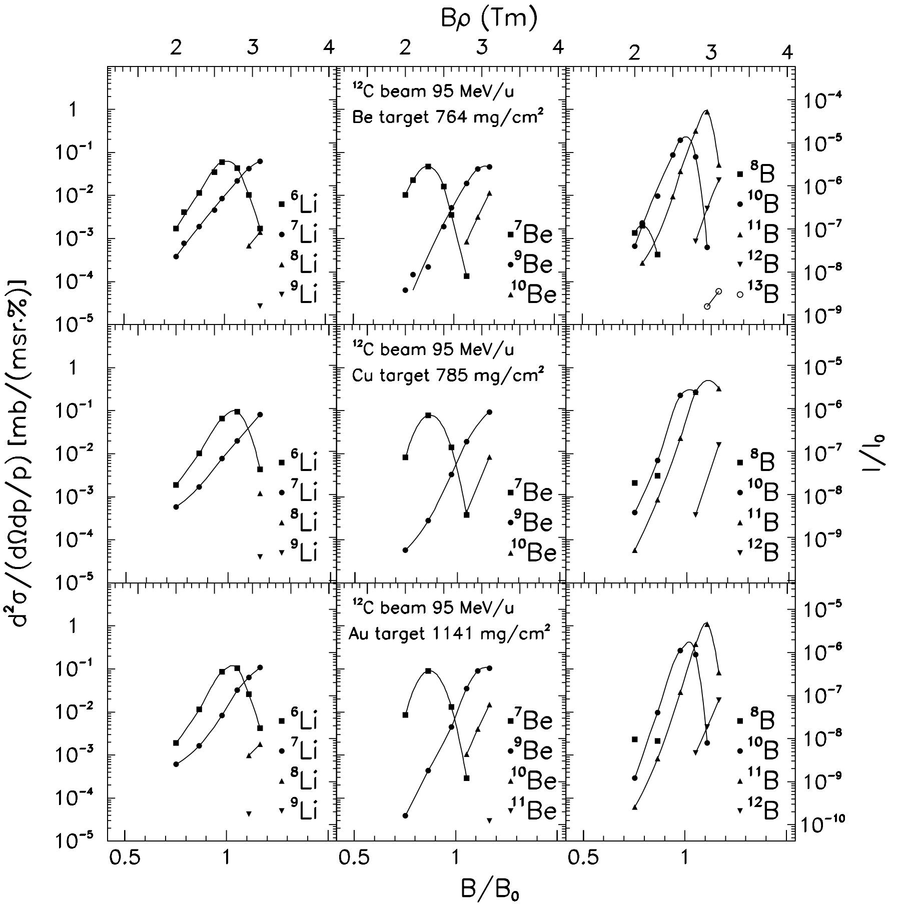

Fig. 11. Comparison of the yields for Li, Be and B isotopes produced from the interaction of 95 MeV/u ^{12}C ions with Be, Cu and Au targets of equivalent thickness (corresponding to an energy loss equal to about 15% of the incident beam energy). The individual production yields I/I_0 and double differential production cross-sections are plotted as a function of B/B_0 and $B\rho$. Same symbols as in fig. 3.

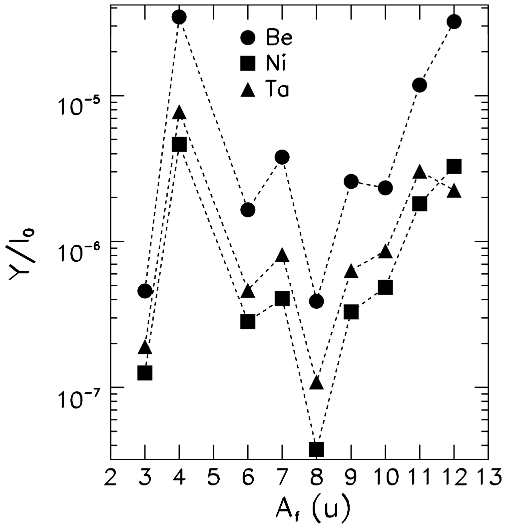

Fig. 12. Variation of the secondary-beam production rate *versus* the fragment mass, for a ^{13}C primary beam and targets of 44 mg/cm^2 Be, 32 mg/cm^2 Ni and 133 mg/cm^2 Ta. The production yield corresponding to the final mass A_f, integrated over the fragment velocity ($B\rho$) and summed over the fragment atomic number Z_f, is plotted *versus* A_f. The lines are drawn to guide the eye.

loss. As was inferred from fig. 11, the production cross-sections, which are plotted in fig. 13 are almost equivalent for the three targets. One can even remark that the highest cross-sections correspond to the Ta target, and the lowest to the Be one in agreement with the variation of the geometric cross-section of these nuclei.

Similar conclusions can be drawn about the results obtained with the ^{12}C projectile.

3.3.3 Influence of the target thickness

The fragment production is expected to increase almost linearly when the target thickness is increased. But the secondary-beam production yield also depends on the spectrometer transmission which is limited by its angular and momentum acceptance. For this reason, after a linear increase, the total production yield saturates and finally decreases when the target thickness is increased. This decrease for very thick targets is mainly due to the broadening of the momentum distribution and to the increase of angular straggling. This effect has already been discussed in ref. [23]. For a given target thickness, the

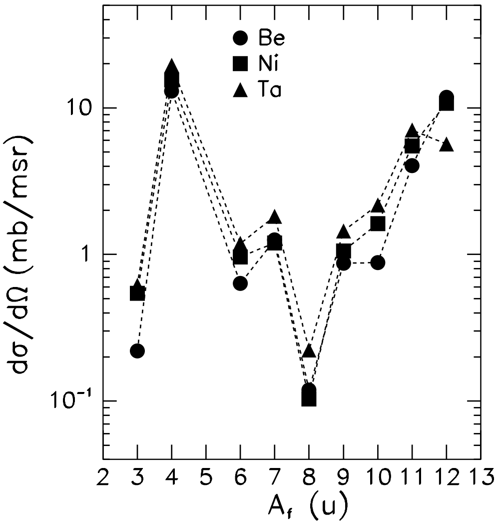

Fig. 13. Variation of the differential cross-section $\mathrm{d}\sigma/\mathrm{d}\Omega$ for fragment production at zero degrees *versus* the fragment mass. Same conditions and symbols as in fig. 12.

maximum production which can be reached depends on the slit aperture. As this parameter also governs the beam selectivity, and as the $B\rho$ distributions obtained may overlap significantly with each other, a compromise has to be found between a good fragment selection and a maximum transmission. If additional discrimination is available in the spectrometer, as is the case for LISE [24], the maximum secondary-beam production will be obtained for a full slit aperture. In these conditions (full slit aperture), the variations of the production yields *versus* target thickness for several secondary beams are shown in fig. 14, for Be, Cu and Au targets. As expected, after an initial increase, the curves exhibit a flat maximum. The decreasing part is not reached here, the targets used for these experiments being not thick enough. Nevertheless, these curves can be used to define the optimum target thickness which corresponds to the thinnest target for which the maximum yield value is reached, or nearly reached. From the data obtained in this work, some of which are presented in fig. 14, one can estimate to about 1000 mg/cm^2 the optimum target thickness for 95 MeV/u ^{12}C when the targets are Be or Cu, and to about 1500 mg/cm^2 the value corresponding to the same beam and Au targets. When the beam is ^{13}C, at 75 MeV/u, the optimum target thickness increases from about 700 to 900 mg/cm^2 from Be to Ta targets. These values are in good agreement with the yield calculations performed using the LISE code (see below).

4 Comparison with the LISE code

4.1 The LISE code

The experimental data from this work, concerning fragment production at zero degrees under various experimental conditions can be compared to the predictions of the

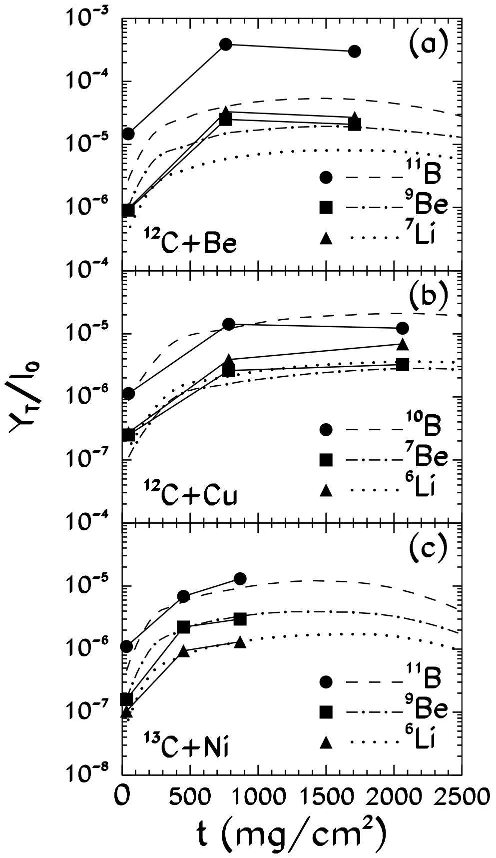

Fig. 14. Influence of the target thickness on the production rate. The yields Y_t/I_0 corresponding to specific secondary beams and to the maximum slit aperture of LISE ($\Delta p/p = 5.97\%$) are plotted *versus* the target thickness, for ^{12}C + Be, Cu and Au targets.

LISE simulation code [25]. This code has been developed at GANIL (Caen, France) to calculate the yields of fragments produced and transmitted in an achromatic spectrometer. It has been regularly improved and is available on the net [26]. The LISE 5.00 version of this code was used for comparison with the present data. The very recent one (LISE 6.00) introduces no significant modification in the fundamental characteristics which will be discussed below.

This simulation takes into account all the aspects of the physical phenomena involved in the production of radioactive beams, to deliver *in fine* the momentum distribution of ionised fragments of given A and Z reaching the focal plane of the spectrometer. The basic inputs are the cross-sections for fragment production at forward angles, the initial fragment momentum distribution, the stopping powers ot targets and absorbers —if any— and the optical parameters of the spectrometer. Among these ingredients, those corresponding to the nuclear reaction itself —fragment cross-section and initial momentum distribution— are the less well known, particularly at energies lower than 100 MeV/u. The problems arising with these "basic" parameters are presented below.

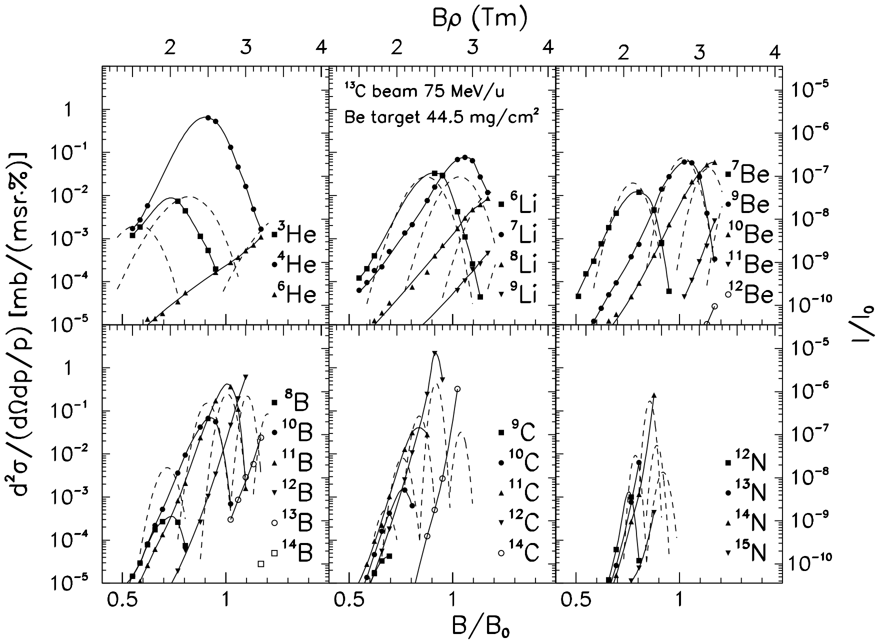

Fig. 15. Comparison of the experimental differential cross-sections and production rates with the results of the LISE simulation for the reactions induced by a ^{13}C beam at 75 MeV/u with a 44 mg/cm^2 Be target. The solid lines are drawn to guide the eye, the dotted ones represent the results from the simulation code. The abscissa and ordinates are as in fig. 4.

4.1.1 Fragmentation cross-sections

In the standard LISE procedure, the fragmentation cross-sections are taken from the empirical parametrization EPAX, which was published initially by Sümmerer *et al.* [27], and recently modified by Sümmerer and Blank [28] to take into account new experimental data obtained with high-energy heavy-ion beams. This parametrization is in good agreement with the data, but, as specified by the authors, the formula are only valid in the so-called "limiting fragmentation" regime, *i.e.* at incident energies well over the Fermi energy, which lies at about 40 MeV/u. This is certainly not the case for the data presented here. As an alternative, the LISE code offers the possibility of introducing the experimental cross-section for a given nuclear reaction. However, this possibility was not used here, as the purpose of this work was to test the standard procedure.

4.1.2 Momentum distributions

The LISE code proposes four different parametrizations to calculate the average momentum of the fragment, and as many possibilities for calculating the fragment momentum width. As far as this last parameter is concerned, only one of them, introduced recently by Tarasov, involves the convolution of a Gaussian with an exponential, and it was obvious that it should be chosen for reproducing the low-energy tails observed in the present data. The parameters used are the default parameters of the code (σ = 91.5 MeV/c, energy from $Q_{\rm gg}$, coef = 3.344, shift = 0.158, the notations being those of refs. [25,26]).

In figs. 15, 16, the experimental momentum distributions obtained for various isotopes produced through ^{12}C + Be and ^{13}C + Be reactions in targets of different thicknesses are compared to the calculations from the LISE code. As one can see from these figures, the calculated curves reproduce the experimental distributions fairly well, and particularly their width, the position of their maxima, and the low-energy tails. Concerning the values of the maximum differential cross-sections shown in fig. 15, the results from the calculations with the LISE code agree within a factor of 2 with the data corresponding to the isotopes ^{6}Li, ^{7,9}Be, ^{11}B and probably ^{10}Be. This agreement can be considered as satisfactory, if one takes into account the fact that we are out of the limits of applicability of the EPAX parameterization. It is therefore not surprising that much larger deviations are observed for most of the other nuclides, and that the agreement is very poor for some of them. In particular, and this is the most important remark from a practical point of view, the yields of the very neutron-deficient nuclei, such as ^{8}B and ^{9}C, are strongly overestimated by the calculation. This may be due to an intense nucleon evaporation combined with the low binding energy of these fragments. This defect of the code for fragments far from the stability line, mentioned in ref. [25], is the most striking evidence that the domain studied here is out of the range —in energy and projectile mass— of the EPAX parametrisation. It is on this point that the future efforts for improving the LISE code should concentrate, and the present data provide a basis for such improvements.

One can see also in figs. 15, 16 that the productions of ^{3}He and ^{4}He are underestimated by the calculation. This is a minor remark, in the scope of secondary-beam production, as these stable beams can easily be obtained directly, but may be of some importance in the scope of

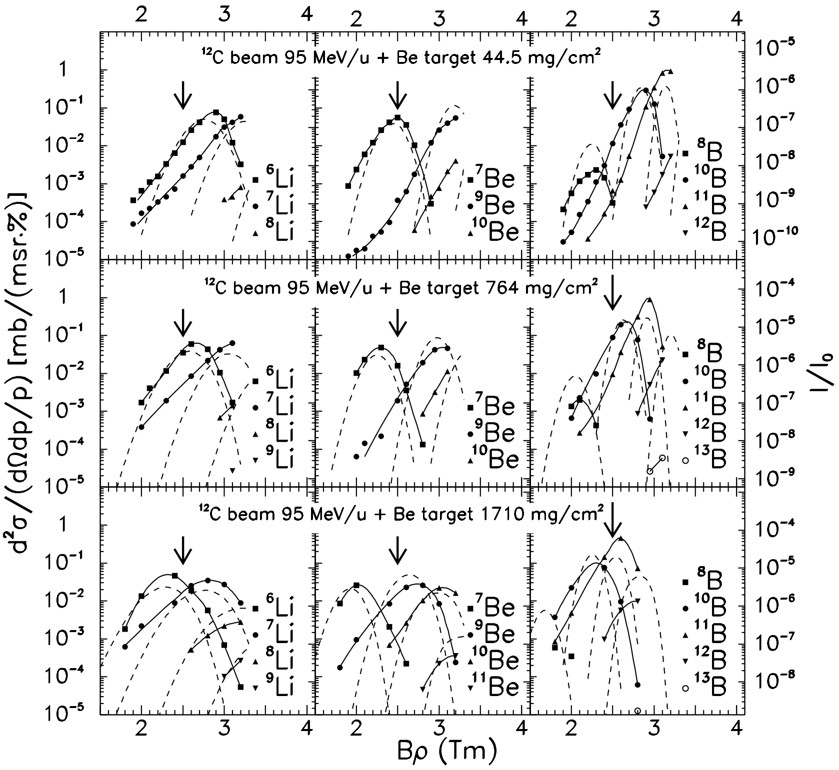

Fig. 16. Same as fig. 15, for a 95 MeV/u ^{12}C beam impinging on Be targets of various thicknesses.

radiotherapy using carbon beams, as these secondary particles have a range exceeding that of the primary beams, and may cause dose deposit beyond the Bragg peak, such effect being sometimes very harmful. From the physics point of view, the underestimation of the ^{3}He and ^{4}He experimental production can easily be explained, as the code does not take into account the emission of these particles through evaporation or direct processes like the break-up into alpha-particles of ^{8}Be in its groundstate, or of ^{12}C in an excited state.

Finally, as mentioned in refs. [25] and [28], the contribution of transfer reactions are not included in the EPAX parametrisation, and this may explain the underestimation of ^{12}C production from ^{13}C, and of ^{11}B production from ^{12}C (see fig. 16).

The LISE code has also been used in this work to simulate the effect of target thickness on fragment production for several isotopes. The result of this calculation is compared to the experimental data in fig. 14. One can see that the general trend of the curves is correctly reproduced, and that the LISE code can be used successfully to determine the optimum target thickness for radioactive beam production.

5 Summary and conclusion

A set of experimental data, concerning the differential cross-sections and production rates at 0°, have been obtained for peripheral collisions induced by ^{12}C and ^{13}C beams of intermediate energy in targets from Be to Au. These data are in good agreement with what is known about the reaction mechanisms at these energies. They have been used to derive general trends concerning secondary-beam production and to test the last version of the LISE code.

The momentum distributions at zero degrees are well reproduced by a function which includes two components, a Gaussian, centred aroud a velocity close to that of the projectile, as in the Goldhaber model, and a low-energy tail which reveals a contribution of dissipative processes. This contribution is less significant when the fragment mass is close to the projectile one.

The comparison of these data with the last version of the LISE code confirms that this simulation code predicts rather well the production cross-sections for fragments, especially close to the stability line. However, significant differences between the data and the LISE predictions — sometimes more than a factor of ten— are found when the fragments are far from the stability line. Unfortunately, these fragments are often the most interesting in the scope of radioactive beam production for nuclear structure or reaction mechanism studies. This work gives the basis for a better parametrisation of cross-sections in this energy range.

The study of the influence of the projectile nature on the fragment production yields shows unambiguously that the ^{13}C projectile favours the production of neutron-rich isotopes. As far as the target nature and thickness are concerned, the maximum production yields are obtained for all kinds of fragments by using a Be target, the thickness of which should be optimised according to the momentum acceptance of the spectrometer (slit aperture) and to the primary-beam nature and energy. For the beams used in this work, the optimum thicknesses of this beryllium target are approximately equal to 1000 mg/cm^2 (95 MeV/u ^{12}C) and 700 mg/cm^2 (75 MeV/u ^{13}C). The knowledge of these values and of the production curves constitute an efficient guide for radioactive nuclear beam production through projectile fragmentation.

We thank the GANIL crew for their cooperation and D. Bazin and C. Stephan for their help in one of the experiments.

References

1. H.H. Heckman, D.E. Greiner, P.J. Lindstrom, F.S. Bieser, Phys. Rev. Lett. **28**, 926 (1972).
2. Y.P. Viogy *et al.*, Phys. Rev. Lett. **42**, 33 (1979).
3. D. Guerreau, V. Borrel, D. Jacquet, B. Gatty, X. Tarrago, Phys. Lett. B **131**, 293 (1983).
4. A.S. Goldhaber, Phys. Lett. B **53**, 306 (1974).
5. D.E. Greiner, P.J. Lindstrom, H.H. Heckman, Bruce Cork, F.S. Bieser, Phys. Rev. Lett. **35**, 152 (1975).
6. V. Borrel, D. Guerreau, J. Galin, B. Gatty, D. Jacquet, X. Tarrago, Z. Phys. A **314**, 191 (1983).
7. B. Borderie, M.F. Rivet, L. Tassan-Got, Ann. Phys. (Paris) **15**, 287 (1990).
8. G. Farès, Thesis UNSA, Nice (1995).
9. P. Delbourgo-Salvador, Report CEA/CE Bruyères-le Châtel, DO.0051/PTN-643/95 (1995).
10. R. Bimbot *et al.*, Report IPNO-DRE-96-18 (1996).
11. S. Belahbib, Thesis, Nice (1999).
12. R. Bimbot *et al.*, Report IPNO-DR-02-009 (2002).
13. M. Bajard, J. Rémillieux, Cah. Radiol., no. 12 (2001); J.M. De Conto, *Proceedings of the 8th European Particle Accelerator Conference (EPAC 2002), Paris, 2002* (CERN and EPS-IGA, Paris, 2002) p. 2727.
14. R. Bimbot *et al.*, Z. Phys. A **322**, 443 (1985).
15. R. Bimbot *et al.*, J. Phys. C **4**, 241 (1986).
16. R. Anne, D. Bazin, A.C. Mueller, J.C. Jacmart, M. Langevin, Nucl. Instrum. Methods A **257**, 215 (1987).
17. G. Bertsch, Phys. Rev. Lett. **46**, 472 (1981).
18. Cheuk-Yin Wong, K. Van Bibber, Phys. Rev. C **25**, 2990 (1982).
19. K. Van Bibber, D.L. Hendrie, D.K. Scott, H.H. Weiman, L.S. Schroeder, J.V. Geaga, S.A. Cessin, R. Treuhaft, Y.J. Grossiord, J.O. Rasmussen, C.Y. Wong, Phys. Rev. Lett. **43**, 840 (1979).
20. R. Legrain, Nucl. Phys. A **387**, 219c (1982).
21. D.L. Silk, H.D. Holmgren, D.L. Hendrie, T.J. M. Symons, G.D. Westfall, P.H. Stelson, S. Raman, R.L. Auble, J.R. Wu, K. Van Bibber, Phys. Rev. C **37**, 158 (1988).
22. M.C. Mermaz, V. Borrel, D. Guerreau, J. Galin, B. Gatty, Z. Phys. A **324**, 217 (1986).
23. R. Bimbot, IPNO-DRE-87-35.
24. R. Anne, A.C. Mueller, Nucl. Instrum. Methods B **70**, 276 (1992).
25. D. Bazin, O. Tarasov, M. Lewitowicz, O. Sorlin, Nucl. Instrum. Methods A **482**, 314 (2002).
26. Web sites: `http://www.ganil.fr/LISE` and `http://www.nscl.msu.edu/~bazin/LISE.html`.
27. K. Sümmerer, W. Brüchle, D.J. Morrissey, M. Schädel, B. Szweryn, Yang Weifan, Phys. Rev. C **42**, 2546 (1990).
28. K. Sümmerer, B. Blank, Phys. Rev. C **61**, 034607 (2000).